Lithium Argyrodite as Solid Electrolyte and Cathode Precursor for Solid-State Batteries with Long Cycle Life

Shuo Wang, Mingxue Tang, Qinghua Zhang, Baohua Li, Saneyuki Ohno, Felix Walther, Ruijun Pan, Xiaofu Xu, Chengzhou Xin, Wenbo Zhang, Liangliang Li, Yang Shen, Felix H. Richter, Jürgen Janek,* and Ce-Wen Nan*

HPSTAR
1272-2021

All-solid-state batteries with conversion-type cathodes promise to exceed the performance of lithium-ion batteries due to their high theoretical specific energy and potential safety. However, the reported performance of solid-state batteries is still unsatisfactory due to poor electronic and ionic conduction in the composite cathodes. Here, in situ formation of active material as well as highly effective ion- and electron-conducting paths via electrochemical decomposition of $Li_6PS_5Cl_{0.5}Br_{0.5}$ (LPSCB)/multiwalled carbon nanotube mixtures during cycling is reported. Effectively, the LPSCB electrolyte forms a multiphase conversion-type cathode by partial decomposition during the first discharge. Comprehensive characterization, especially *operando* pressure monitoring, reveals a co-redox process of two redox-active elements during cycling. The monolithic LPSCB-based cell shows stable cycling over 1000 cycles with a very high capacity retention of 94% at high current density (0.885 mA cm^{-2}, ≈0.7 C) at room temperature and a high areal capacity of 12.56 mAh cm^{-2} is achieved.

1. Introduction

All-solid-state batteries (ASSBs) have attracted much attention due to their expected safety and high specific energy.[1–3] Most ASSB concepts rely on replacing the (flammable) liquid electrolyte by solid electrolyte and the graphite anode by lithium metal, while retaining a layered transition metal oxide as cathode material.[4–10] Additionally, the introduction of conversion-type cathode materials into ASSBs could further increase the specific energy substantially.[11] However, the morphological, structural, and chemical changes during cycling are highly complex[12] and the cycling performance of ASSBs at room temperature (RT) with conversion-type cathode materials, such as S, FeS_2, or Li_2S, is not yet satisfactory.[13–15]

Whereas liquid electrolyte can easily infiltrate the porous cathode composite to homogeneously contact active material particles and form a fast ion transport network, this is more difficult to achieve in ASSBs.[16,17] The effective ionic and electronic partial conductivities are often much lower than expected, especially in conversion-type cathodes due to poor ionic/electronic conductivity of many conversion-type cathode materials and high tortuosity factors.[18,19] Therefore, high fractions of solid electrolytes and carbon additives are used to increase ionic and electronic conduction, respectively, at the cost of lowering the areal capacities of the cells.[20–24]

Although many conversion-type ASSBs were reported with high specific capacities (normalized to the mass of active material) at RT, they often have low areal capacities (mostly

Dr. S. Wang, C. Xin, Prof. L. Li, Prof. Y. Shen, Prof. C.-W. Nan
State Key Laboratory of New Ceramics and Fine Processing
School of Materials Science and Engineering
Tsinghua University
Beijing 100084, China
E-mail: cwnan@mail.tsinghua.edu.cn
Dr. S. Wang, Prof. S. Ohno,[+] F. Walther, Dr. R. Pan, Dr. W. Zhang,
Dr. F. H. Richter, Prof. J. Janek
Institute of Physical Chemistry and Center for Materials Research
Justus-Liebig-University Giessen
Heinrich-Buff-Ring 17, D-35392 Giessen, Germany
E-mail: juergen.janek@phys.chemie.uni-giessen.de

(iD) The ORCID identification number(s) for the author(s) of this article can be found under https://doi.org/10.1002/aenm.202101370.

Prof. M. Tang
Center for High Pressure Science and Technology Advanced Research
Beijing 100094, China
Prof. Q. Zhang
Beijing National Laboratory for Condensed Matter Physics
Institute of Physics
Chinese Academy of Sciences
Beijing 100190, P. R. China
Prof. B. Li, X. Xu
Engineering Laboratory for the Next Generation Power
and Energy Storage Batteries
Graduate School at Shenzhen
Tsinghua University
Shenzhen 518055, China

<1 mAh cm^{-2}) owing to low active material loading.[13–15,25–31] Several ASSBs with conversion-type cathodes exhibit high areal capacities (up to 4 mAh cm^{-2}), but these degrade rapidly during cycling.[32–34] Good cycling performance was only reported at relatively low current densities (<0.4 mA cm^{-2}).[35–38] Elevated temperatures (≥60 °C) were needed to obtain high C-rate performance.[20,39,40] With increasing areal capacity, higher current densities are required to maintain the same C-rate, but the obtained capacity declines due to poor ionic/electronic transport pathways and high electrode overpotential. Therefore, achieving high areal capacity and sufficient ionic/electronic transport pathways is essential.[2]

The formation of redox-active cathode material in situ by decomposition of the solid electrolyte at the surface of electron-conducting carbon networks is a promising approach. Usually considered a major drawback of thiophosphate solid electrolytes, their reduction and oxidation at moderately low and high potentials may actually be an opportunity if the formed decomposition products can be controlled. Designing optimized solid electrolyte/carbon composites as "precursors" may open a route toward electrochemically highly active and reversible conversion-type cathodes.[38,41,42] So far, the Li_6PS_5Cl and Li_6PS_5Br solid electrolytes used as precursors for the in situ formation of active material showed unsatisfactory cycling performance.[43–45] Moreover, only few reports try to elucidate the complex electrochemical reaction mechanism.[38,41–45] For example, it has recently been reported that in the Li_6PS_5Cl-C composite cathode Li_6PS_5Cl decomposes upon initial reduction into LiCl, Li_2S and Li_3P, which could be then oxidized into S and $P_2S_7^{4-}$ during a full charge step.[45] Moreover, in situ pressure measurements have been utilized to monitor lithiation/delithiation of intercalation-type cathodes.[46,47] However, using *operando* pressure

measurements to understand the possible reaction pathways of conversion-type cathodes has not been reported yet.

In the following, we report that ASSBs with $Li_6PS_5Cl_{0.5}Br_{0.5}$ (LPSCB) and multiwalled carbon nanotubes (MWCNTs) as cathode, LPSCB as solid electrolyte and In/InLi as anode (i.e., In/InLi | LPSCB | LPSCB-MWCNTs cells) offer a stable areal capacity of 1.24 mAh cm^{-2} at 0.7 C over 1000 cycles. Partial decomposition of LPSCB by electrochemical reduction during the first discharge step forms redox-active compounds in situ, and the remaining, unchanged LPSCB electrolyte provides low-impedance ionic transport pathways in the composite cathode. Comprehensive advanced analytical techniques, especially *operando* pressure analysis, reveal the electrochemical reaction mechanism. The in situ formed composite cathode and its 3D network of solid electrolyte, carbon and active material offer a stable and high capacity in ASSBs.

2. Results and Discussion

2.1. Design and In Situ Formation of the Composite Cathode

In the composite cathode, LPSCB acts as both electrolyte and precursor for redox-active material (see **Figure 1a**), as described above. More details about the LPSCB electrolyte are shown in Figures S1 and S2 and Table S1 in the Supporting Information. Figure 1b shows a typical scanning electron microscopy (SEM) image of a cross-section of the monolithic ASSB cells including the cathode and electrolyte layers. The uniform sulfur and chlorine signals identified by energy dispersive X-Ray (EDX) spectroscopy throughout the cross-section before cycling indicate that the LPSCB particles
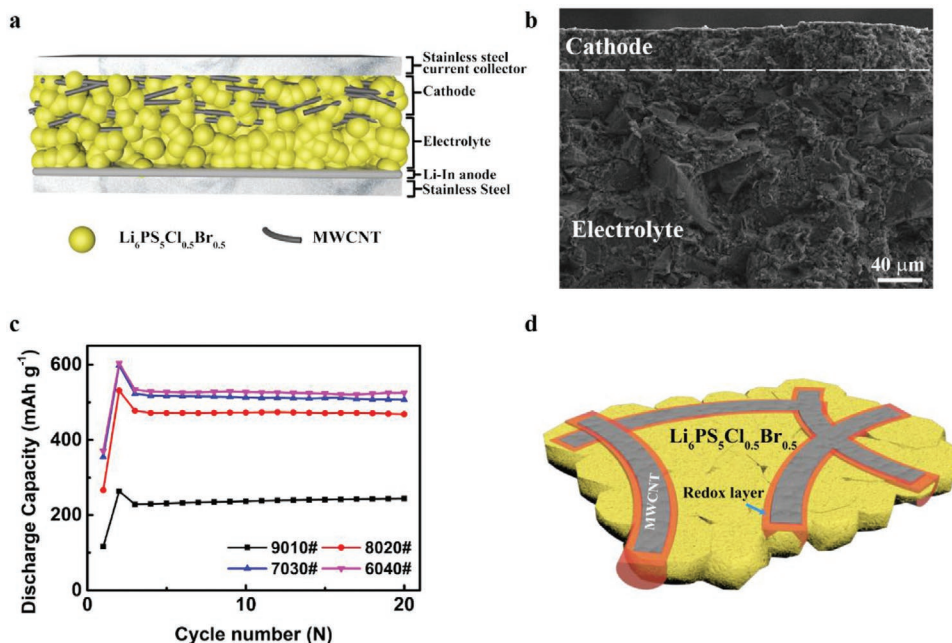

Figure 1. a) Scheme of an In/InLi | LPSCB | LPSCB-MWCNTs cell with monolithic structure. Yellow spheres and dark short rods represent LPSCB particles and MWCNTs, respectively. b) Cross-sectional SEM image of the ASSB including cathode and electrolyte layers. c) Cycling performance of LPSCB-based ASSBs with 10, 20, 30, and 40 wt% MWCNTs in the composite cathodes. d) Schematic illustration of the LPSCB-MWCNTs composite electrode. Black, orange, and yellow colored regions indicate MWCNTs, redox layer, and LPSCB, respectively.

are well-distributed across the cathode and electrolyte layers (Figure S3, Supporting Information). Cathode, solid electrolyte and anode layers are tightly contacted, even up to 24.8 mg cm^{-2} of LSPCB loading of the cathode (Figure S4, Supporting Information). The high-magnification SEM image of the cathode before cycling (Figure S5, Supporting Information) shows that some MWCNTs interconnect in the cathode and form effective electronic conduction pathways.

The MWCNTs are tightly covered with LPSCB due to ball milling (Figure S6, Supporting Information). Samples with 10, 20, 30, and 40 wt% MWCNTs (corresponding to 11.5, 22.6, 33.3, and 43.8 vol%) in the LPSCB-MWCNTs composite are named as 9010#, 8020#, 7030#, and 6040#, respectively. The cycling performance of the cathodes with different ratios of LPSCB to MWCNTs is shown in Figure 1c. To simplify the capacity calculation, the specific capacity throughout the present work was calculated based on the total mass of LPSCB in the composite cathode. The discharge capacity increases, first steeply, then slowly, with increasing MWCNT content (Figure S7, Supporting Information). This indicates that only those electrolyte particles in contact with MWCNTs participate in the formation of active material (Figure 1d). Based on the measured capacity of 1.78 mAh after 20 cycles, about 34% LPSCB in the composite cathode decomposes and the thickness of the resulting redox-active layer is roughly 13% of the radius of LPSCB particles (see Note S1 in Supporting Information). Thus, the composite cathode is formed in situ via electrochemical decomposition of a part of LPSCB in the LPSCB-MWCNTs composite layer.

2.2. Electrochemical Reaction Mechanism of the LPSCB-MWCNTs Cathode

To reveal the reversible redox reaction mechanism of the LPSCB-MWCNTs composite cathodes, ex situ X-ray photoelectron spectroscopy (XPS), nuclear magnetic resonance (NMR), Auger electron spectroscopy (AES), X-ray diffraction (XRD), scanning transmission electron microscopy (STEM), and *operando* pressure measurements were performed to characterize the 7030# cathode at various states during cycling. **Figure 2a** shows the discharge–charge voltage profile. The discharge/charge current density was 0.044 mA cm^{-2} for the first two cycles and 0.176 mA cm^{-2} for the following cycles in a voltage range of 0–3 V. Unless stated otherwise, we reference the potential versus In/InLi.

XRD patterns (Figure 2b) of the composite cathode at different charge/discharge states show that there are no other well-defined diffraction peaks in addition to the diffraction peaks assigned to crystalline LPSCB. After charging the cell to 3 V in the second cycle, no significant changes of the diffraction pattern are observed (Figure 2b). Upon subsequent discharge of the electrode to 0 V, a broad reflection at a 2θ value of about 27° (as indicated by yellow region) appears, which is attributed to the formation of amorphous Li$_2$S.[22]

In order to elucidate the decomposition products of the LPSCB-MWCNTs cathode at different stages, ex situ XPS was conducted (see Figure 2c,d and Figure S8, Supporting Information). For the LPSCB electrolyte, the PS$_4^{3-}$ and free-S^{2-} ions are attributed to the Li$_6$PS$_5$Cl$_{0.5}$Br$_{0.5}$ phase.[23,48,49] After mixing with

MWCNTs by ball-milling (pristine cathode), a slight increase in intensity of P-S-P (such as P$_2$S$_7^{4-}$, P$_2$S$_6^{2-}$, and P$_2$S$_6^{4-}$) and S$_x$ signals was observed.[50–52]

The S 2p spectrum obtained after the initial discharge to 0.6 V is similar to that for the pristine cell due to no obvious capacity delivered at this stage. However, with further reduction to 0 V, the P-S-P and S$_x$ doublets disappear, the PS$_4^{3-}$ signals decrease and the S^{2-} signals increase. These changes indicate the reductive decomposition of LPSCB, leading to the formation of Li$_2$S.[23] At the same time, a new shoulder in the P 2p spectrum at ≈128.5 eV appears, indicating the formation of reduced phosphorous-containing species (P/Li$_x$P).[53]

When subsequently charging the cell to 2 V, the Li$_2$S signals decrease and the P/Li$_x$P signal contributions disappear. Meanwhile, the PS$_4^{3-}$ signals in the S 2p spectrum become more pronounced and the P-S-P signals reappear in both S 2p and P 2p spectra. In addition, the S$_x$ signals appear.[50] Various compounds besides elemental sulfur lie in this binding energy range for thiophosphates, such as different long chain polysulfides.[50,52] Therefore, we use the simplified term "S$_x$ species" for the products upon charging. Upon further oxidation to 3 V versus In/InLi, the PS$_4^{3-}$ signals decrease and the Li$_2$S signals fully disappear, while the P-S-P and S$_x$ signals continue to increase. Overall, the observations upon oxidation suggest the formation of lithium thiophosphate phases from Li$_2$S and P/Li$_x$P, and their subsequent oxidation to S$_x$ species.

For the second cycle (Figure 2c,d), when the cell is discharged again to 0.6 V, the S$_x$ signals disappear, accompanied by a decrease in the P-S-P signal contributions, and the PS$_4^{3-}$ signals rise again. Also, the Li$_2$S signals slightly increase. When the cell is fully discharged to 0 V in the second cycle, the P-S-P signal contributions almost disappear, and the Li$_2$S doublet continues to increase. The detail spectra after 20 cycles show that the spectral changes during charge and discharge are reproducible, which already indicates a high degree of reversibility of the occurring reactions.

However, it is not possible to confirm unequivocally the presence of LiCl and LiBr phases after the decomposition of LPSCB with XPS (Figure S8, Supporting Information), due to small binding energy differences of Cl (Br) in LPSCB and LiCl (LiBr).[54] From AES measurements, we assume that the formation of LiCl is part of the decomposition reaction in the LPSCB-MWCNTs cathode (see Figures S9–S11, Supporting Information). To further support the hypothesis of LiCl formation, we performed STEM-EDX measurements of particles originating from the cathode after discharge to 0 V in the second cycle (Figures S12 and S13, Supporting Information), and the results illustrate the presence of LiCl in the composite cathode. Because both Br and Cl occupy the same 4a and 4c site in the structure of LPSCB,[55] we assume that LiBr is also a decomposition product of LPSCB.

Furthermore, solid-state NMR spectroscopy was conducted to get further information about the reaction pathway of LPSCB-MWCNTs electrodes, as displayed in **Figure 3**. In the pristine LPSCB electrolyte, most lithium ions are connected to the PS$_4^{3-}$ tetrahedra.[44] One small shoulder is found at around 2 ppm, which can be assigned to the free S^{2-} in the argyrodite structure.[45] The ball-milled composite cathode displays a much broader line compared to the pristine LPSCB electrolyte due to the increased fraction of glass phase containing PS$_4^{3-}$ (Figure 3c and Figures S14–S16, Supporting Information).
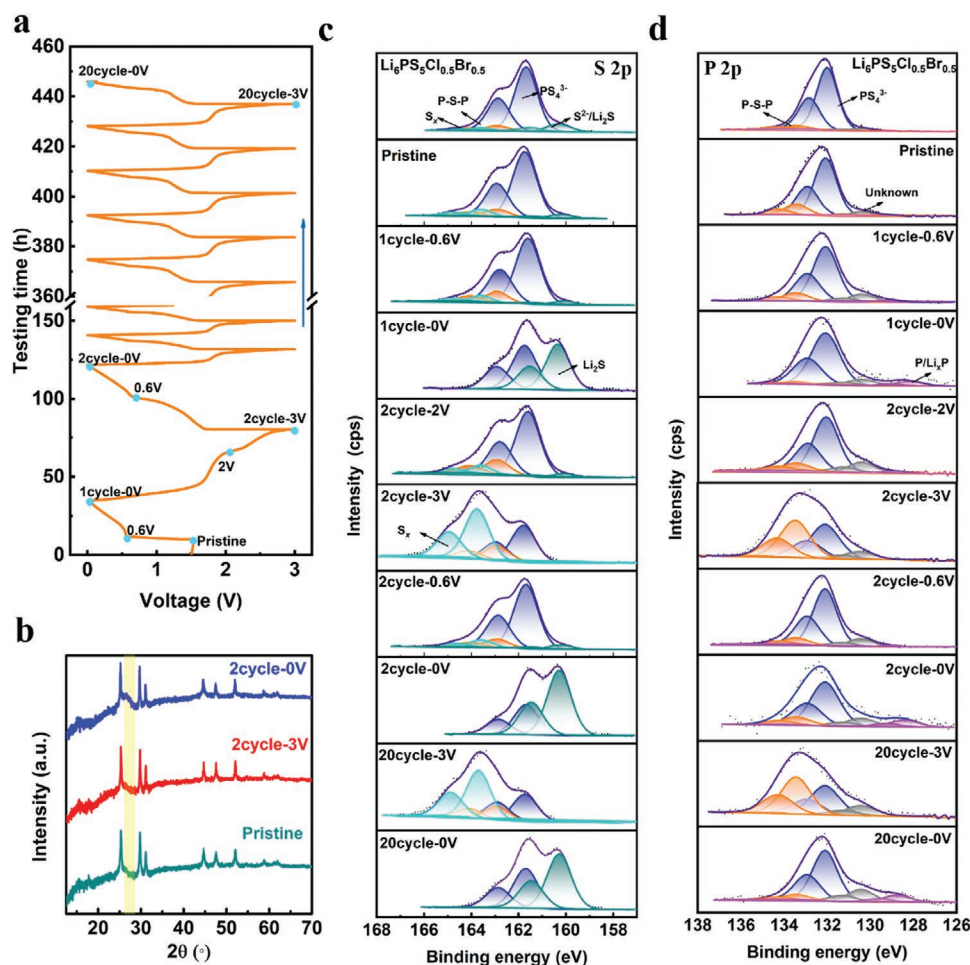
Figure 2. a) Discharge–charge voltage profile (vs In/InLi) for ASSBs with 30 wt% MWCNTs in the LPSCB-MWCNTs composite. b) Ex situ XRD patterns of the 7030# cathode at different states during cycling. Normalized XP spectra of c) S 2p and d) P 2p of the 7030# cathode at different states during cycling. The cyan-colored dots in Figure 2a indicate the states at which the ex situ analyses were carried out. In S 2p spectra, there are four doublets providing clues of underlying electrochemical reactions upon cycling, which are S^{2-} (≈160.2 eV, dark-green doublet), PS_4^{3-} (≈ 161.7 eV, dark-blue doublet), P-S-P (≈162.9 eV, orange doublet), and S_x (≈ 163.6 eV, light-blue doublet). Since the peak split of S 2p was constrained to be 1.18 eV for all signal fits, the reported doublet positions correspond to the energetic signal positions of the respective S $2p_{3/2}$ signal contribution. For the P 2p spectra, the doublets of PS_4^{3-} (≈ 132.1 eV, dark-blue doublet), P-S-P (≈ 133.5 eV, orange doublet), and reduced phosphorous species (≈ 128.5 eV, purple doublet) are visible upon cell cycling. Since the typical binding energy range of elemental phosphorous is in the range of ≈ 130 eV,[53] we assume the reduced phosphorus species to be P/Li_xP. As expected, the PS_4^{3-} and P-S P doublets in the S 2p and P 2p spectra show the same trend. Thus, the P 2p spectra confirm the observations made with S 2p.

The cycled LPSCB-MWCNTs cathodes show an additional broadening at the tail centered at ≈87 ppm, which is assigned to isolated PS_4^{3-} tetrahedra.[44] In the ^6Li and ^7Li NMR spectra of the cathode charged to 2 V in the second cycle, a residual broad signal between 0.5 and −2 ppm is observed for the irreversible LiCl/LiBr formed in the first cycle (Figure 3a,b). Meanwhile, resonance signals in the range > 90 ppm appear (Figure 3c), indicating the oxidation of the PS_4^{3-} phases into various possible anionic frameworks. The signal at > 90 ppm in the ^{31}P spectrum indicates the formation of $P_2S_7^{4-}$,[45] while the weak signal at ≈115 ppm can be attributed to a tiny amount of $P_2S_6^{2-}$.[51,56] When the composite cathode is further charged to 3 V, a deeper oxidation from PS_4^{3-} to $P_2S_7^{4-}$, $P_2S_6^{2-}$ and amorphous S_x occurs, confirming the XPS results.

After discharging to 0.6 V in the second cycle, the signal at > 90 ppm in the ^{31}P spectra decreases, reflecting the reduction of the various anionic frameworks, such as $P_2S_6^{2-}$ and

$P_2S_7^{4-}$. Simultaneously, a broad signal between 1 and −2 ppm shows up in ^7Li spectra, indicating the formation of PS_4^{3-} and LiCl/LiBr, color-marked in Figure 3a.[45,57] Upon further discharging to 0 V, both broad resonances (the purple-filled area) in ^7Li and ^6Li NMR grow in intensity, indicating Li_2S is formed (Figure 3a,b).[58] The reduced products of P^0 and Li_xP with lower fractions of x here are reflected by ^{31}P spectra for the cathode discharged to 0 V (Figure 3c and Figure S17, Supporting Information).[59] However, the reduced product Li_3P is not obvious at −270 ppm in ^{31}P spectra for the cathode discharged to 0 V (Figure S17, Supporting Information),[59] which might be due to the insufficient amount of Li_3P for NMR detection in this study.

The pressure changes upon cycling were monitored through an *operando* pressure measurement shown in **Figure 4**. The net-pressure change Δp of a full cell is typically governed by the volume changes of both the cathode and anode materials. Therefore, the pressure test can also be used to reveal the
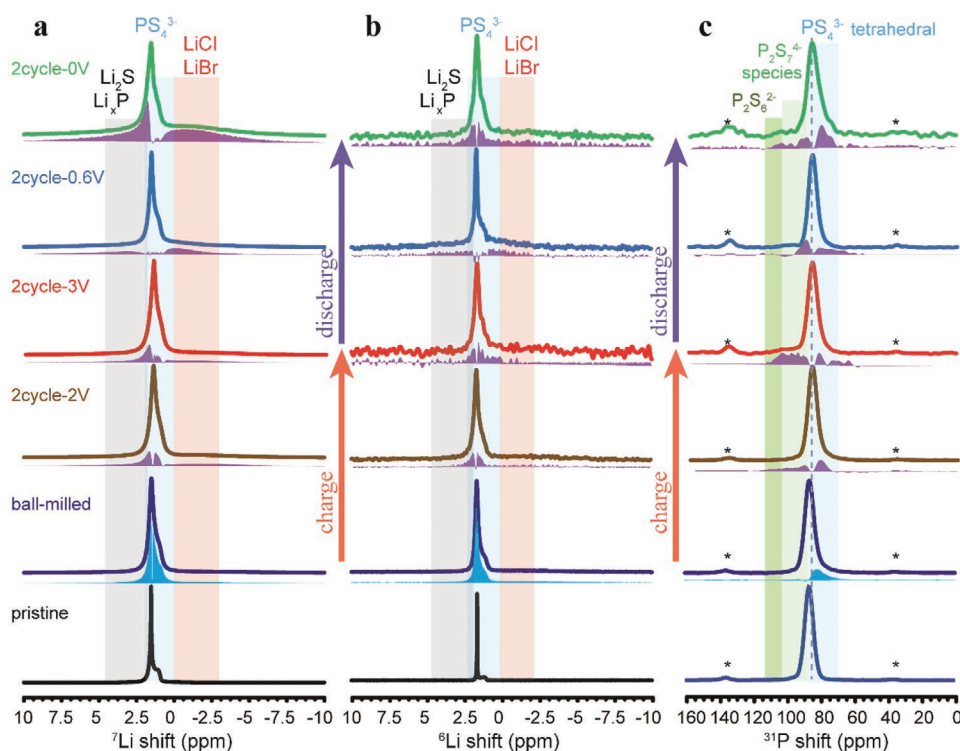
Figure 3. Ex situ high-resolution solid-state NMR spectra of LPSCB electrodes at different states of cycling for a) ^{7}Li, b) ^{6}Li, and c) ^{31}P isotope. The cycled cathodes are chosen from the cycling curve shown in Figure 2a. The difference between the pristine LPSCB electrolyte (black spectra) and the ball-milled LPSCB-MWCNTs composite cathode (dark purple spectra) is marked as light blue-filled areas. The differences between the cycled electrodes and the pristine LPSCB-MWCNTs composite cathode are presented as the purple-filled areas. In order to better compare the evolution upon cycling, all differences are magnified (doubled).
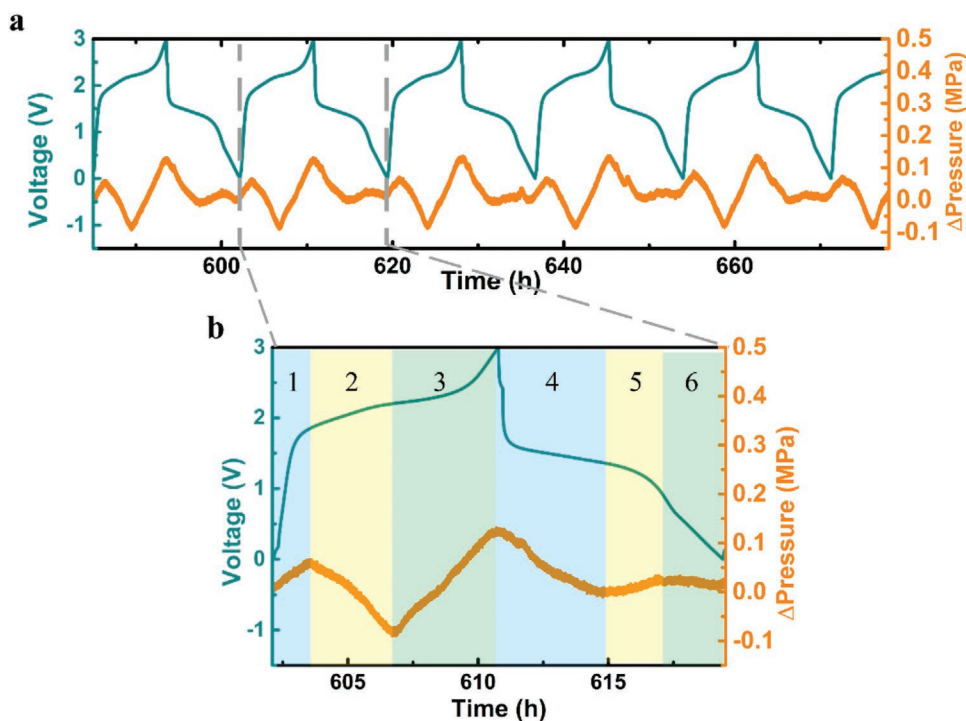

Figure 4. a) Exemplary potential profile combined with the in situ measured cell pressure change in relation to the pressure of the cell before charging. b) Magnification of the data for one cycle. Six regions can be distinguished in each cycle based on the potential profile and the pressure change.

complex conversion reaction during cycling. While simple conversion reactions such as In + Li$^+$ + e$^-$ → InLi should result in a linear volume increase, the observed Δp profiles show a non-linear behavior with three distinct regions (regions 1–3) upon charging (Figure 4b). In other words, there are at least three different reactions involved in the cathode side, each with a specific volume change.

The theoretical volume change associated with a chemical reaction of a conversion-type material, i.e., the molar reaction volume $\Delta_r \overline{V}_m$, can be estimated on the basis of crystallographic information.[46] We estimated the volume changes for the aforementioned reaction steps in Figure 4b during charging. We assumed that the PS$_4^{3-}$-rich phase, which is formed by a reaction of Li$_2$S and P^0 (Li$_x$P is not taken into account here), can be represented by (Li$_2$S)$_{0.75}$(P$_2$S$_5$)$_{0.25}$, which is subsequently converted to (Li$_2$S)$_{0.67}$(P$_2$S$_5$)$_{0.33}$ (representing Li$_4$P$_2$S$_7$, P$_2$S$_7^{4-}$) and finally to (Li$_2$S)$_{0.50}$(P$_2$S$_5$)$_{0.50}$ (representing Li$_2$P$_2$S$_6$, P$_2$S$_6^{2-}$).[51] Accordingly, the corresponding reaction volumes can be calculated as follows:

Reaction (1)—Li$_3$PS$_4$ (LPS) phase formation

$$\Delta_r \overline{V}_m \left[4\text{Li}_2\text{S} + \text{P} \rightarrow 2(\text{Li}_2\text{S})_{0.75}(\text{P}_2\text{S}_5)_{0.25} + 5\text{Li}^+ + 5\text{e}^- \right]$$
$$= -5.60 \, \text{cm}^3 \, \text{mol}^{-1} \tag{1}$$

Reaction (2)—LPS oxidation I

$$\Delta_r \overline{V}_m \left[4(\text{Li}_2\text{S})_{0.75}(\text{P}_2\text{S}_5)_{0.25} \rightarrow 3(\text{Li}_2\text{S})_{0.67}(\text{P}_2\text{S}_5)_{0.33} + \text{S} + 2\text{Li}^+ + 2\text{e}^- \right]$$
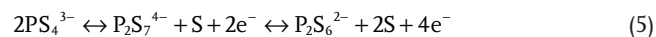$$= -8.50 \, \text{cm}^3 \, \text{mol}^{-1} \tag{2}$$

Reaction (3)—LPS oxidation II

$$\Delta_r \overline{V}_m \left[3(\text{Li}_2\text{S})_{0.67}(\text{P}_2\text{S}_5)_{0.33} \rightarrow 2(\text{Li}_2\text{S})_{0.50}(\text{P}_2\text{S}_5)_{0.50} + \text{S} + 2\text{Li}^+ + 2\text{e}^- \right]$$
$$= -5.76 \, \text{cm}^3 \, \text{mol}^{-1} \tag{3}$$

Considering $\Delta_r \overline{V}_m$(In/InLi) = +7.89 cm^3 mol^{-1}, only reaction (2) can lead to a decrease in Δp upon charging. Accordingly,

we assume that the oxidation of the LPS glass phases starts in region 2 (Figure 4b). Consequently, the formation of the LPS glass phases takes place in region 1. Although the complete reaction pathway is more complex and convoluted, the above-mentioned simplified reactions and their reaction volumes can well explain the observed trend in Δp, further confirming our hypothesis regarding the reaction mechanism. A more comprehensive list of possible reactions and associated reaction volumes is listed in Tables S2 and S3 in the Supporting Information. The slightly more moderate changes of Δp in regions 4–6 are likely due to the more sluggish lithium-ion transport in the composite after oxidation. As recently reported, the effective conductivity in the composite can be significantly lower after applying a sufficiently high potential.[60] Region 4 is wider than region 3, indicating the overlapping reaction especially in regions 4 and 5, which may also account for the moderate Δp changes during the discharge process. However, it remains to confirm the reaction pathways of lithium thiophosphates during the discharge process. The results highlight the benefit of *operando* pressure measurements to better understand complex conversion reactions.

Overall, the results of the various analytical investigations above are in very good agreement with each other, which allows us to propose an underlying reaction mechanism within the conversion-type composite cathode (**Figure 5**). The major reactions contributing to the reversible capacity are

$$4\text{S}^{2-} + \text{P}^{x-} \leftrightarrow \text{PS}_4^{3-} + (5+x)\text{e}^- \tag{4}$$

$$2\text{PS}_4^{3-} \leftrightarrow \text{P}_2\text{S}_7^{4-} + \text{S} + 2\text{e}^- \leftrightarrow \text{P}_2\text{S}_6^{2-} + 2\text{S} + 4\text{e}^- \tag{5}$$

We assume that LPSCB decomposes during the first discharge, forming Li$_2$S, Li$_x$P, and LiCl/LiBr. LiCl(LiBr) is electrochemically inactive once it is formed and does not contribute to the reversible capacity. In the following charging process, PS$_4^{3-}$ units are formed again. At higher potentials, oxidized sulfur species (P$_2$S$_7^{4-}$, P$_2$S$_6^{2-}$, S$_x$) are increasingly formed. Assuming S^0 and P$_2$S$_5$ as the "ideal" oxidation products for the sake of
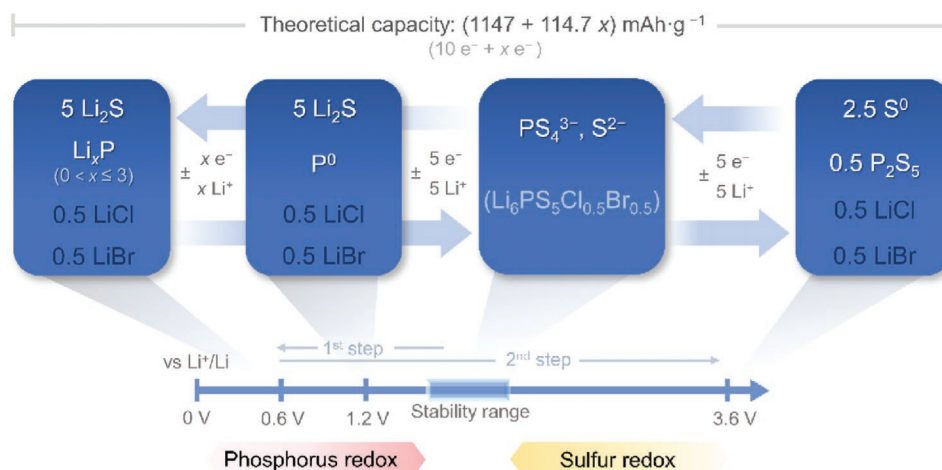

Figure 5. The sulfur and phosphorus redox reactions are exploited during cell operation. Upon the initial discharge ("formation step", 1st step), the LPSCB argyrodite decomposes into Li$_2$S, reduced phosphorous species (P^0/Li$_x$P) and LiCl/LiBr. The darker text color of LiCl/LiBr indicates that these species are inactive in the redox process. Upon charging (2nd step), Li$_3$PS$_4$(LPS)-like phases are formed first, which then decompose to oxidized sulfur species. Note that we assume "theoretical" products S^0 and P$_2$S$_5$ here to describe the underlying reactions in a simplified way.

simplicity, the process from S^0 and P_2S_5 to Li_2S and Li_xP comprises $10 + x$ electrons and $10 + x$ Li^+ ions, which corresponds to a theoretical capacity of $(1147 + 114.7x)$ mAh g^{-1}. Considering Li_3P ($x = 3$), this ultimately leads to a maximum theoretical capacity of 1491.1 mAh g^{-1}. Thus, the charge/discharge process of our conversion-type composite cathode utilizes both sulfur and phosphorus redox activity, i.e., a co-redox process of two redox-active elements is achieved.

2.3. Cell Performance and Benchmarking

High room-temperature cycling performance is important for practical application of ASSBs. The electrochemical performance of LPSCB based ASSBs with 7030# cathode is shown in **Figure 6**. As shown in Figure 6a, the cell with 3.1 mg cm^{-2} LPSCB cathode loading delivers a stable discharge capacity of 524 mAh g^{-1} at

0.176 mA cm^{-2} after 400 cycles without any degradation. A high Coulombic efficiency of around 100% is shown from the fourth cycle on, which demonstrates that the decomposition products of LPSCB show reversible electrochemical activity. When the cell is cycled at 0.442 mA cm^{-2}, the discharge capacity increases and then stabilizes at 539 mAh g^{-1} after 500 cycles (Figure 6b). This gradual increase in the discharge capacity after activation process (Figure 6b) is due to the increase in room temperature induced by seasonal variation from spring to summer during the long-term cell cycling. Even at a higher current density of 0.885 mA cm^{-2}, the cell still presents excellent long-term cycling performance. The specific capacity initially decreases, then increases, and finally stabilizes at about 402 mAh g^{-1} (equivalent to 1.24 mAh cm^{-2}) after 1030 cycles with a high capacity retention of 94% (Figure 6c), demonstrating its excellent long-term cycling stability. The rate test demonstrates the equally excellent rate performance of the cells (Figure S18, Supporting Information).
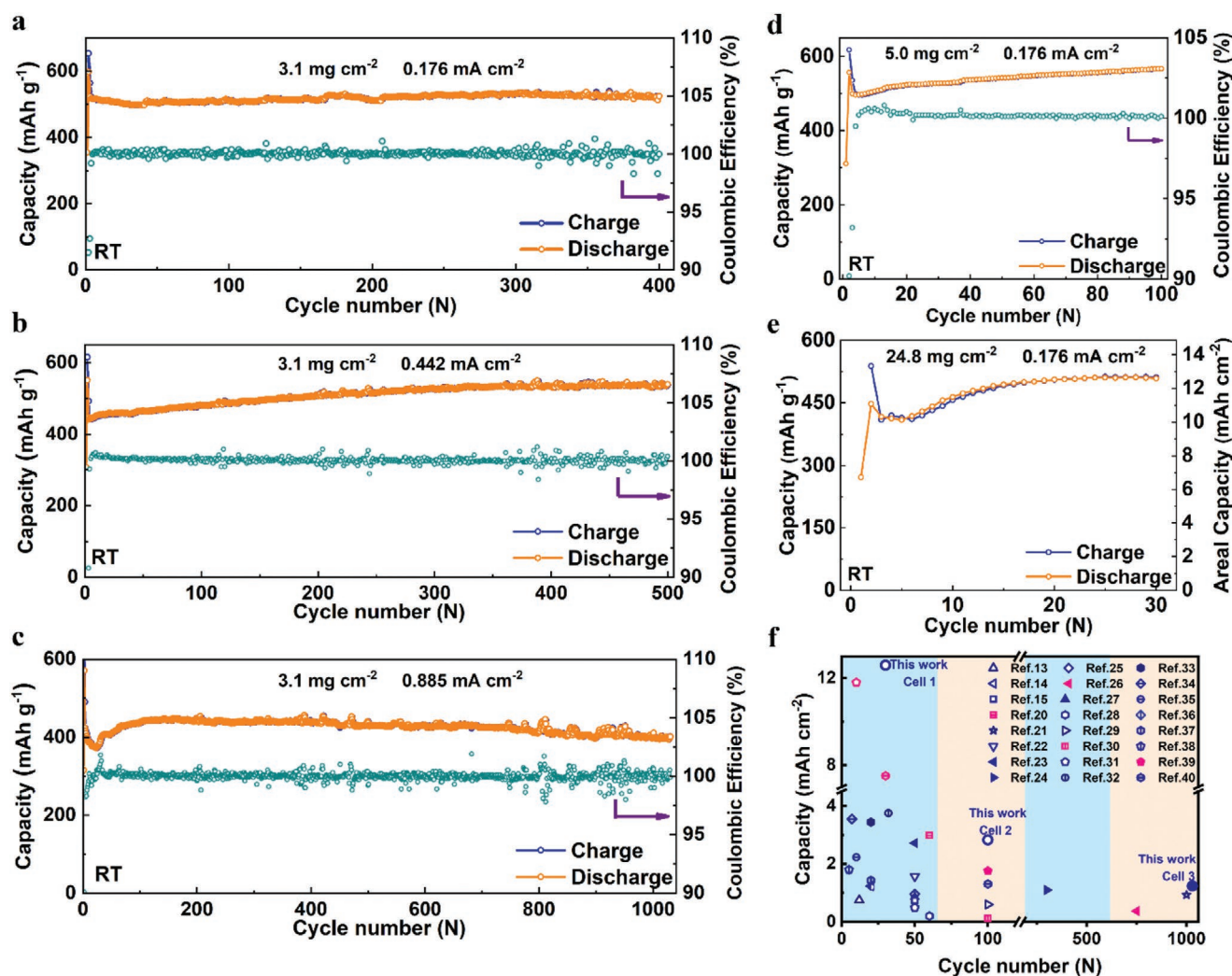

Figure 6. Cycling performance of an ASSB cell with LPSCB cathode loading of 3.1 mg cm^{-2} at different current densities of a) 0.176 mA cm^{-2}, b) 0.442 mA cm^{-2}, and c) 0.885 mA cm^{-2} at RT, with different cathode LPSCB loadings of d) 5.0 mg cm^{-2} and e) 24.8 mg cm^{-2} at 0.176 mA cm^{-2} at RT. f) Comparison of the state of the art areal capacities and cycling performance for ASSBs with different sulfur-based conversion-type cathodes. Filled symbols indicate current density of cycling cells (> 0.5 mA cm^{-2}). Empty symbols indicate current density of cycling cells (≤ 0.5 mA cm^{-2}). Pink symbols indicate the cells cycled at 60 °C. Royal symbols indicate the cells cycled at RT or 25 °C.

2101370 (7 of 10)

Increasing the areal capacity is one of the key factors to increase specific energy and energy density of ASSBs to fulfill commercial requirements. Figure 6d shows the cycling performance of the cell with LPSCB cathode loading of 5.0 mg cm^{-2} at 0.176 mA cm^{-2} at RT. The capacity increases initially and stabilizes at 566.8 mAh g^{-1} (equivalent to 2.81 mAh cm^{-2}). At almost fivefold LPSCB cathode loading of 24.8 mg cm^{-2}, a reversible capacity of about 508.5 mAh g^{-1} at the 30th cycle (equivalent to 12.6 mAh cm^{-2}) at 0.176 mA cm^{-2} is achieved (Figure 6e). The areal capacity of the cell is among the highest reported sulfur-based conversion-type cathodes for ASSBs (Figure 6f and Table S4, Supporting Information). This cell shows an exceptionally high hypothetical specific energy of the composite cathode (669 Wh kg^{-1}, see Table S5, Supporting Information), which is higher than most intercalation-type cathodes (Figure S19, Supporting Information), but the hypothetical energy density does not have a similar advantage (Figure S20 and Table S6, Supporting Information).[2]

No apparent overpotential increase occurs during cycling, which guarantees good cycling performance of the cells with high active material loading (Figure S21, Supporting Information). In particular, the cell resistance (< 20 Ω cm^2) is very low, which allows the excellent cycling performance and the high capacity retention of ASSBs (Figures S22 and S23 and Table S7, Supporting Information). From the focused ion beam (FIB)-SEM cross-section image of the cells, the cathode becomes denser compared to the pristine cathode and the interface between the cathode and electrolyte remains intimately contacted, which accounts for the stable cycling of the cell (Figure S24, Supporting Information). The cells with a cathode LPSCB loading of 4.7 mg cm^{-2} can deliver a stable discharge capacity of 419.3 mAh g^{-1} after 400 cycles at a large current density of 2.55 mA cm^{-2} at 60 °C, demonstrating superior long-term cycling performance for LPSCB-based ASSB at elevated temperature (Figure S25, Supporting Information).

3. Conclusions

In summary, we have achieved a high areal capacity of up to 12.56 mAh cm^{-2} at RT by utilizing the sulfur and the phosphorus redox activity of the decomposition products of "precursor" LPSCB solid electrolyte as active materials in ASSBs ("two-element redox"). Due to the well-designed composite cathode structure and the application of external pressure to the cells, the LPSCB-based cells can deliver around 1.24 mAh cm^{-2} after 1030 cycles at a large current density of 0.885 mA cm^{-2} at RT with a high capacity retention of 94%. The major reactions contributing to the reversible capacity have been revealed by complementary characterization methods. Accordingly, LPS-like phases are decomposed to Li$_2$S and P/Li$_x$P during discharge. During charge, the reduction products are oxidized to LPS-like phases, containing various polyanions such as P$_2$S$_7^{4-}$ and P$_2$S$_6^{2-}$ and S$_x$-like species. LiCl and LiBr are irreversibly formed during the first discharge process. Our work deepens the understanding of the electrochemical reaction of thiophosphate solid electrolytes and opens a new avenue for developing high-performance ASSBs. This method could also be extended to other argyrodite-type thiophosphate solid electrolytes.

4. Experimental Section

Synthesis: Li$_6$PS$_5$Cl$_{0.5}$Br$_{0.5}$ was prepared by solid-state reaction. Li$_2$S (Alfa, 99.9%), LiCl (Aladdin, 99.9%), LiBr (Aladdin, 99%), and P$_2$S$_5$ (Aladdin, 99%) powders were weighed in the appropriate stoichiometric ratio and mixed by ball milling at 100 rpm for 2 h using a planetary ball mill (Fritsch Pulverisette 7). Subsequently, the mixture was sealed in a quartz tube, annealed at 550 °C for 10 h, and then slowly cooled to RT.

The raw MWCNTs (Shenzhen Nanotech Port Co. Ltd., China) were pretreated with nitric acid as reported in a previous publication.[21] The composite cathode was obtained by ball milling the mixture of LPSCB and MWCNTs at 300 rpm for 1 h. All procedures were conducted under argon atmosphere in a glove box ([O$_2$] < 1 ppm, [H$_2$O] < 1 ppm).

Characterization: The cross-sectional morphology and composition of the samples were examined by SEM (Zeiss Merlin) at an acceleration voltage of 5 kV with EDX at 15 kV. The cross-sectional morphology of the cell after long-term cycling was imaged using the FIB technique (TESCAN, China S9000X). The (120 × 150) μm² crater with 90° was obtained using a xenon source. The dwell time was 1 μs. The samples were transferred using an Ar-filled shuttle to minimize side reactions with air. The FIB-SEM images were obtained at an accelerating voltage of 5 kV. The phase identification of the samples was obtained using an XRD diffractometer (Rigaku D/max-2500 diffraction meter with a Cu K$_\alpha$ radiation source). The samples were sealed in an airtight container covered with a Kapton polyimide thin film to prevent air contamination reactions due to moisture and air. The surface chemistry of the samples was examined using an XPS spectrometer (PHI 5000 VersaProbe II) with a monochromatized Al K$_\alpha$ source (1486.6 eV). The samples were transferred from the glovebox to the analysis chamber using a transfer shuttle filled with Ar gas. The sample surface was cleaned for 3 min via Ar$^+$ sputtering with an acceleration voltage of 2 kV. The suitability of the calibration was double-checked with the binding energies of the main components of the different samples. Common curve fitting restrictions were used such as upper full width at half maximum limits, fixed area ratios (e.g., p orbitals 1:2), and fixed spin–orbit splittings.[53]

AES (PHI-700, ULVAC-PHI) was performed to analyze the elemental distribution of the composite cathode at the fully charged/discharged state. Samples were transferred from the glove box into the instrument using a transfer vessel filled with Ar gas. The morphology of the composite cathode after being fully discharged to 0 V was obtained using a Cs-corrected FEI Titan G2 60-300 kV (Field Electron and Ion Ltd., Hillsboro, USA) TEM with EDX operated at 120 kV. The samples were transferred using an Ar-filled container. Solid-state magic-angle-spinning (MAS) NMR experiments were carried out on a Bruker Avance III-400 spectrometer operating at ^{6}Li, ^{7}Li, and ^{31}P Larmor frequencies of 58.9, 155.5, and 162.0 MHz, respectively. The samples were collected from the cathode layer and a small amount of solid electrolyte layer. All samples were packed into 4.0 mm zirconia rotors in an Argon-filled glovebox to avoid decomposition. The rotors with sample were spun at 8 kHz using a 4.0 mm MAS HX probe. A single pulse sequence was employed for all signal acquisition. The π/2 pulse lengths of 2.0, 0.96, and 0.95 μs were determined for ^{6}Li, ^{7}Li, and ^{31}P detection, respectively. Both ^{6}Li and ^{7}Li shifts were referenced to a 1 mol L^{-1} solution of LiCl at 0 ppm. ^{31}P spectra were externally referenced to 85 wt% H$_3$PO$_{4(aq)}$ at 0 ppm.

Electrochemical Measurements: LPSCB-based ASSBs were assembled as follows. First, 120 mg of LPSCB powder was pressed in a polyetheretherketone housing with a diameter of 12 mm at 120 MPa. Then, the composite cathode was evenly spread onto the electrolyte pellet and pressed at 100 MPa. Afterward, the thin lithium foil was put on the other side of the pellet followed by put an indium foil, the cell was pressed at 150 MPa for 3 min. The ASSBs were tested in a homemade Swagelok cell at a constant pressure of 150 MPa using a LANHE battery testing system (CT3001A, LANHE, China) in a voltage range of 0.0–3.0 V (vs In/InLi), corresponding to 0.6–3.6 V (vs Li$^+$/Li). The current density for all batteries was set as 0.044 mA cm^{-2} for the first two cycles to activate the cathode. All cell cycling at RT was carried out in a glove box. The ac impedance measurement was conducted using an impedance analyzer (ZAHNER-Elektrik, IM6) in the frequency range of

1 MHz to 1 Hz at RT. The *operando* pressure monitoring of the cell with 7030# cathode was conducted with a homemade apparatus. Detailed information about the apparatus is described in the previous works.[46,47] The cell pressure was fixed at around 120 MPa by tightening the frame.

Supporting Information

Supporting Information is available from the Wiley Online Library or from the author.

Conflict of Interest

The authors declare no conflict of interest.

Data Availability Statement

Research data are not shared.

[1] J. Janek, W. G. Zeier, *Nat. Energy* **2016**, *1*, 16141.

[2] S. Randau, D. A. Weber, O. Kötz, R. Koerver, P. Braun, A. Weber, E. Ivers-Tiffée, T. Adermann, J. Kulisch, W. G. Zeier, F. H. Richter, J. Janek, *Nat. Energy* **2020**, *5*, 259.

[3] K. J. Kim, M. Balaish, M. Wadaguchi, L. Kong, J. L. M. Rupp, *Adv. Energy Mater.* **2020**, *11*, 2002689.

[4] S. Wang, X. Zhang, S. Liu, C. Xin, C. Xue, F. Richter, L. Li, L. Fan, Y. Lin, Y. Shen, J. Janek, C.-W. Nan, *J. Materiomics* **2020**, *6*, 70.

[5] H. Huo, Y. Chen, J. Luo, X. Yang, X. Guo, X. Sun, *Adv. Energy Mater.* **2019**, *9*, 1804004.

[6] M. Jia, N. Zhao, H. Huo, X. Guo, *Electrochem. Energy Rev.* **2020**, *3*, 656.

[7] S. Deng, Y. Sun, X. Li, Z. Ren, J. Liang, K. Doyle-Davis, J. Liang, W. Li, M. Norouzi Banis, Q. Sun, R. Li, Y. Hu, H. Huang, L. Zhang, S. Lu, J. Luo, X. Sun, *ACS Energy Lett.* **2020**, *5*, 1243.

[8] C. Wang, J. Liang, Y. Zhao, M. Zheng, X. Li, X. Sun, *Energy Environ. Sci.* **2021**, *14*, 2577.

[9] M. Weiss, F. J. Simon, M. R. Busche, T. Nakamura, D. Schröder, F. H. Richter, J. Janek, *Electrochem. Energy Rev.* **2020**, *3*, 221.

[10] E. Umeshbabu, B. Zheng, Y. Yang, *Electrochem. Energy Rev.* **2019**, *2*, 199.

[11] W. P. Wang, J. Zhang, J. Chou, Y. X. Yin, Y. You, S. Xin, Y. G. Guo, *Adv. Energy Mater.* **2020**, *11*, 2000791.

[12] X. Sun, A. M. Stavola, D. Cao, A. M. Bruck, Y. Wang, Y. Zhang, P. Luan, J. W. Gallaway, H. Zhu, *Adv. Energy Mater.* **2020**, *11*, 2002861.

[13] C. Yu, J. Hageman, S. Ganapathy, L. van Eijck, L. Zhang, K. R. Adair, X. Sun, M. Wagemaker, *J. Mater. Chem. A* **2019**, *7*, 10412.

[14] C. Yu, L. van Eijck, S. Ganapathy, M. Wagemaker, *Electrochim. Acta* **2016**, *215*, 93.

[15] Y. Zhang, R. Chen, T. Liu, Y. Shen, Y. Lin, C. W. Nan, *ACS Appl. Mater. Interfaces* **2017**, *9*, 28542.

[16] K. H. Park, Q. Bai, D. H. Kim, D. Y. Oh, Y. Zhu, Y. Mo, Y. S. Jung, *Adv. Energy Mater.* **2018**, *8*, 1800035.

[17] S. Wang, W. Zhang, X. Chen, D. Das, R. Ruess, A. Gautam, F. Walther, S. Ohno, R. Koerver, Q. Zhang, W. G. Zeier, F. H. Richter, C. W. Nan, J. Janek, *Adv. Energy Mater.* **2021**, *11*, 2100654.

[18] G. F. Dewald, S. Ohno, J. G. C. Hering, J. Janek, W. Zeier, *Batteries Supercaps* **2020**, *4*, 183.

[19] S. Wang, R. Fang, Y. Li, Y. Liu, C. Xin, F. H. Richter, C.-W. Nan, *J. Materiomics* **2021**, *7*, 209.

[20] F. Han, J. Yue, X. Fan, T. Gao, C. Luo, Z. Ma, L. Suo, C. Wang, *Nano Lett.* **2016**, *16*, 4521.

[21] Y. Zhang, T. Liu, Q. Zhang, X. Zhang, S. Wang, X. Wang, L. Li, L.-Z. Fan, C.-W. Nan, Y. Shen, *J. Mater. Chem. A* **2018**, *6*, 23345.

[22] S. Wang, Y. Zhang, X. Zhang, T. Liu, Y. H. Lin, Y. Shen, L. Li, C. W. Nan, *ACS Appl. Mater. Interfaces* **2018**, *10*, 42279.

[23] S. Ohno, R. Koerver, G. Dewald, C. Rosenbach, P. Titscher, D. Steckermeier, A. Kwade, J. Janek, W. G. Zeier, *Chem. Mater.* **2019**, *31*, 2930.

[24] T. Hakari, A. Hayashi, M. Tatsumisago, *Adv. Sustainable Syst.* **2017**, *1*, 1700017.

[25] M. Nagao, Y. Imade, H. Narisawa, T. Kobayashi, R. Watanabe, T. Yokoi, T. Tatsumi, R. Kanno, *J. Power Sources* **2013**, *222*, 237.

[26] X. Yao, N. Huang, F. Han, Q. Zhang, H. Wan, J. P. Mwizerwa, C. Wang, X. Xu, *Adv. Energy Mater.* **2017**, *7*, 1602923.

[27] K. Suzuki, N. Mashimo, Y. Ikeda, T. Yokoi, M. Hirayama, R. Kanno, *ACS Appl. Energy Mater.* **2018**, *1*, 2373.

[28] X. Xu, G. Hou, X. Nie, Q. Ai, Y. Liu, J. Feng, L. Zhang, P. Si, S. Guo, L. Ci, *J. Power Sources* **2018**, *400*, 212.

[29] Y. Lin, X. Wang, J. Liu, J. D. Miller, *Nano Energy* **2017**, *31*, 478.

[30] Z. Lin, Z. Liu, N. J. Dudney, C. Liang, *ACS Nano* **2013**, *7*, 2829.

[31] T. Hakari, M. Nagao, A. Hayashi, M. Tatsumisago, *J. Power Sources* **2015**, *293*, 721.

[32] K. Fu, Y. Gong, G. T. Hitz, D. W. McOwen, Y. Li, S. Xu, Y. Wen, L. Zhang, C. Wang, G. Pastel, J. Dai, B. Liu, H. Xie, Y. Yao, E. D. Wachsman, L. B. Hu, *Energy Environ. Sci.* **2017**, *10*, 1568.

[33] R. Xu, J. Yue, S. Liu, J. Tu, F. Han, P. Liu, C. Wang, *ACS Energy Lett.* **2019**, *4*, 1073.

[34] U. Ulissi, S. Ito, S. M. Hosseini, A. Varzi, S. Aihara, S. Passerini, *Adv. Energy Mater.* **2018**, *8*, 1801462.

[35] M. Nagao, A. Hayashi, M. Tatsumisago, *J. Mater. Chem. A* **2012**, *22*, 10015.

[36] T. Takeuchi, H. Kageyama, K. Nakanishi, M. Tabuchi, H. Sakaebe, T. Ohta, H. Senoh, T. Sakai, K. Tatsumi, *J. Electrochem. Soc.* **2010**, *157*, A1196.

[37] M. Nagao, A. Hayashi, M. Tatsumisago, T. Ichinose, T. Ozaki, Y. Togawa, S. Mori, *J. Power Sources* **2015**, *274*, 471.

[38] F. Han, T. Gao, Y. Zhu, K. J. Gaskell, C. Wang, *Adv. Mater.* **2015**, *27*, 3473.

[39] X. Li, J. Liang, J. Luo, C. Wang, X. Li, Q. Sun, R. Li, L. Zhang, R. Yang, S. Lu, H. Huang, X. Sun, *Adv. Mater.* **2019**, *31*, 1808100.

[40] H. Yan, H. Wang, D. Wang, X. Li, Z. Gong, Y. Yang, *Nano Lett.* **2019**, *19*, 3280.

[41] S. Wang, X. Xu, X. Zhang, C. Xin, B. Xu, L. Li, Y. Lin, Y. Shen, B. Li, C. Nan, *J. Mater. Chem. A* **2019**, *7*, 18612.

[42] Y. Zhang, R. Chen, T. Liu, B. Xu, X. Zhang, L. Li, Y. Lin, C. W. Nan, Y. Shen, *ACS Appl. Mater. Interfaces* **2018**, *10*, 10029.

[43] G. F. Dewald, S. Ohno, M. A. Kraft, R. Koerver, P. Till, N. M. Vargas-Barbosa, J. Janek, W. G. Zeier, *Chem. Mater.* **2019**, *31*, 8328.

[44] D. H. S. Tan, E. A. Wu, H. Nguyen, Z. Chen, M. A. T. Marple, J.-M. Doux, X. Wang, H. Yang, A. Banerjee, Y. S. Meng, *ACS Energy Lett.* **2019**, *4*, 2418.

[45] T. K. Schwietert, V. A. Arszelewska, C. Wang, C. Yu, A. Vasileiadis, N. J. J. de Klerk, J. Hageman, T. Hupfer, I. Kerkamm, Y. Xu, E. van der Maas, E. M. Kelder, S. Ganapathy, M. Wagemaker, *Nat. Mater.* **2020**, *19*, 428.

[46] R. Koerver, W. Zhang, L. de Biasi, S. Schweidler, A. O. Kondrakov, S. Kolling, T. Brezesinski, P. Hartmann, W. G. Zeier, J. Janek, *Energy Environ. Sci.* **2018**, *11*, 2142.

[47] W. Zhang, D. Schröder, T. Arlt, I. Manke, R. Koerver, R. Pinedo, D. A. Weber, J. Sann, W. G. Zeier, J. Janek, *J. Mater. Chem. A* **2017**, *5*, 9929.

[48] R. Koerver, F. Walther, I. Aygün, J. Sann, C. Dietrich, W. G. Zeier, J. Janek, *J. Mater. Chem. A* **2017**, *5*, 22750.

[49] F. Walther, R. Koerver, T. Fuchs, S. Ohno, J. Sann, M. Rohnke, W. G. Zeier, J. Janek, *Chem. Mater.* **2019**, *31*, 3745.

[50] F. Walther, S. Randau, Y. Schneider, J. Sann, M. Rohnke, F. H. Richter, W. G. Zeier, J. Janek, *Chem. Mater.* **2020**, *32*, 6123.

[51] C. Dietrich, D. A. Weber, S. J. Sedlmaier, S. Indris, S. P. Culver, D. Walter, J. Janek, W. G. Zeier, *J. Mater. Chem. A* **2017**, *5*, 18111.

[52] E. Nagai, T. S. Arthur, P. Bonnick, K. Suto, J. Muldoon, *MRS Adv.* **2019**, *4*, 2627.

[53] J. F. Moulder, W. F. Stickle, P. E. Sobol, K. D. Bomben, *Phys. Electron.: Eden Prairie, US-MN* **1995**.

[54] S. Wenzel, S. J. Sedlmaier, C. Dietrich, W. G. Zeier, J. Janek, *Solid State Ionics* **2018**, *318*, 102.

[55] M. A. Kraft, S. P. Culver, M. Calderon, F. Bocher, T. Krauskopf, A. Senyshyn, C. Dietrich, A. Zevalkink, J. Janek, W. G. Zeier, *J. Am. Chem. Soc.* **2017**, *139*, 10909.

[56] S. Neuberger, S. P. Culver, H. Eckert, W. G. Zeier, J. Schmedt, A. d. Gunne, *Dalton Trans.* **2018**, *47*, 11691.

[57] K. H. Shigenobu Hayashi, *Bull. Chem. Soc. Jpn.* **1990**, *63*, 913.

[58] M. U. Patel, I. Arcon, G. Aquilanti, L. Stievano, G. Mali, R. Dominko, *ChemPhysChem* **2014**, *15*, 894.

[59] M. Mayo, K. J. Griffith, C. J. Pickard, A. J. Morris, *Chem. Mater.* **2016**, *28*, 2011.

[60] S. Ohno, C. Rosenbach, G. F. Dewald, J. Janek, W. G. Zeier, *Adv. Funct. Mater.* **2021**, *31*, 2010620.